Plastic hexahedral FEM for surgical simulation

Ruiliang Gao[1] and Jörg Peters[1*]

[1*]University of Florida, Gainesville, 32611, FL, USA.

*Corresponding author(s). E-mail(s): jorg.peters@gmail.com;
Contributing authors: rgao15@ufl.com;

Abstract

Purpose: Soft-tissue manipulations, such as collecting, stretching or tearing tissue, are a common component of surgery. When too much force is applied, these manipulations result in a residual plastic deformation that surgeons should be aware of and that should be modeled by surgical simulation.

Methods: Many tissues, vessels and organs can be modeled as offsets of curved simple shapes with primary directions, e.g., radial and axial for cylinders yield a rectangular mesh whose normal offset naturally yields a hexahedral mesh that can serve as a thick shell. Other organs are easy to embed into and deform following a hex mesh. We extend existing code for the volumetric finite element method (FEM) to model tissue plasticity as hexahedral thick shells or embedded organs. Specifically, the work extends the open source Simulation Open Framework Architecture (SOFA) and its newest hyperelastic deformation addition, Caribou, with focus on surgical simulation. The extension factors deformation gradients into (corotational or hyperelastic) elastic factors and plastic factors and enforces volume preservation. Limits on per-element twist, twist torque, material hardening and bounds on plasticity where elements invert avoid the need for re-meshing.

Results: Our hexahedral FEM avoids the biased outcomes of asymmetric coarsely-partitioned tetrahedral FEM. Caribou's hyperelastic FEM is extended to hex-FEM stretching plasticity. Our high-order accurate blended-vertex deformation enables coarse hex meshes to model large plastic rotational and stretch deformations without re-meshing. We compare a vertex-blended to a cell-centered piecewise constant approach; contrast plasticity based on corotational FEM and hyperelastic FEM;

and test the computation under mesh refinement. The volume is preserved also for large deformations.

Conclusion On-the-fly generated hexahedral meshes can directly be used as finite element domains for plastic deformation based on corotational or hyperelastic elasticity. The outcome is suitable for surgical simulation.

Keywords: hyperelasticity, plasticity, tissue, surgery simulator, laparoscopic.
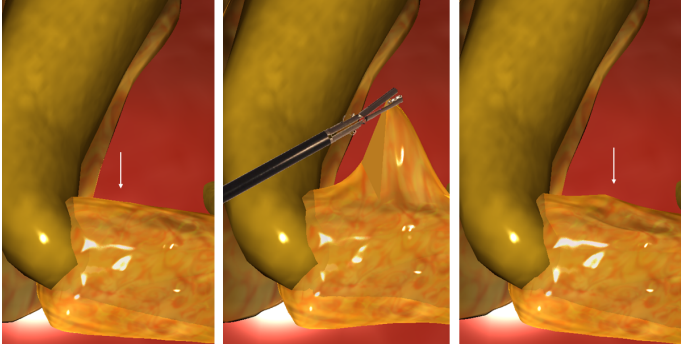

Fig. 1: Laparoscopic surgery simulation: excessive stretching of fatty tissue with a grasper results in a vestigial plastic deformation at ↓

1 Introduction

Internal soft tissue holds vessels and organs in place. Skillful removal, e.g. by tearing such tissue, is an important surgical skill that requires appropriate approach and force. Beyond a level of force, the tissue does not return to its initial position after release. Realistic simulation of tissue manipulation should therefore model plastic deformation. Over-stretching of tissue or organ walls must be monitored and displayed, e.g. as vestigial plastic deformation, see Fig. 1, to teach correct surgical technique.

The Simulation Open Framework Architecture (SOFA) [2] and its recently added Caribou component [3] offer corotational elastic, respectively hyperelastic deformations (that can handle elastoplastic deformation under larger strain) but plastic deformations currently only for linear tetrahedral-based finite elements. Algorithmically-generated tetrahedral meshing is subject to strong changes in layout, already for small changes of the enclosing surface. Luckily, for most tissues required for surgical simulation, it is therefore natural and efficient to generate meshes as an offset from a quadrilateral (curved) base surface: For example, fatty tissue can often be presented by offsetting a curved quadrilateral grid, see Fig. 3 (b); and thick-walled organs, say of the gastrointestinal tract or blood vessels, naturally have cylindrical structure, see Fig. 1. Fig. 3b shows an organ embedded into a free-from 'morphing' (deformation)
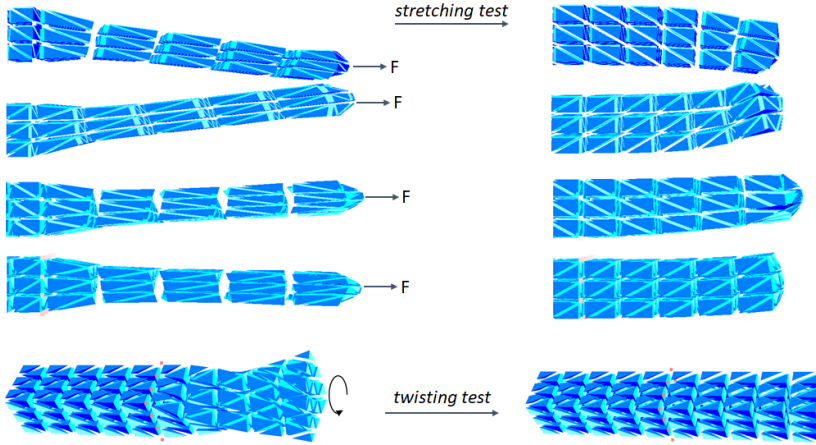
Fig. 2: Plastic deformation, SOFA tet-elements: stretch (top four) lacks symmetry. Twisting (bottom) lacks plasticity. (left) initial (right) final deformation; see also [1].

grid of hexahedra. Such embedding is readily available in SOFA and can be computed, for example, via polycube maps [4]. All cases yield an immediate, low-cost, predictable approximation via a hexahedral mesh.

To apply SOFA's existing algorithms for plasticity to real-time simulation of soft tissue, in the laparoscopic training environment Toolkit for Illustration of Procedures in Surgery (TIPS) [5] split the naturally arising hexahedra into tetrahedra. This resulted in excessive stiffness, see Fig. 2, *top*; and asymmetry, when tessellating minimally, hence asymmetrically, see Fig. 2, *bottom*. The point is that splitting a natural hexahedral mesh into tets is fraught with problems even when, as in the example, the tetrahedralization has a good aspect ratio.
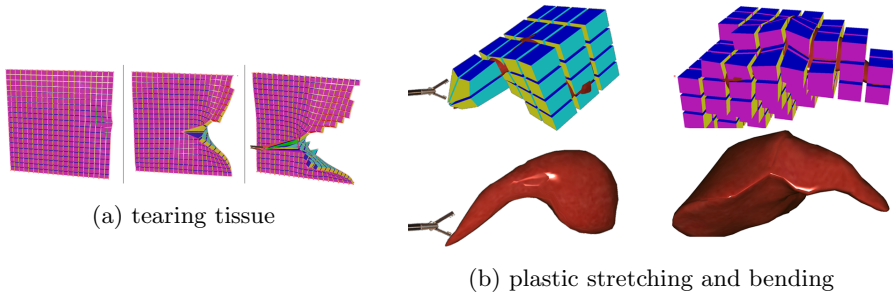

(a) tearing tissue

(b) plastic stretching and bending

Fig. 3: Models for interactive surgical training. (a) Tearing a peritoneal sheet. (b) Free-form deformation cage of hexahedra enclosing the liver.

While tet-meshes typically lack the feature alignment and symmetry of offset-generated hex elements there is currently no *hex*-FEM code available for modeling plasticity in an interactive surgery simulation environment. This paper describes a SOFA-extension to plastic FEM using hexahedral elements. Our 'blended-vertex approach' carefully calibrates higher accuracy and simplicity of computation for real-time applications. An extension of SOFA to hex-based linear co-rotational elasto-plastic FEM, and to third-order accurate blended-vertex deformation [6] to hex meshes was introduced in our MICCAI contribution [7]. The latter can model large plastic deformations by regularly-arranged coarse hex meshes instead of high-resolution irregular tet meshes. For completeness, we review the underlying plastic decomposition scheme for stretching and rotational plasticity and the trade-off between the piecewise constant, cell-centered, plastic rotational deformation and our 'blended vertex' deformation. The new contributions are:

- addition of a refinement test to characterize rotational plastic deformation based on corotational elasticity;
- extending the stretching plasticity deformation to hyperelastic FEM provided by Caribou, while preserving the volume also for large deformations, and
- comparing plastic stretching when the underlying elastic model is hyperelastic vs the corotational model.

Note that we do not apply the approach of [6] to elastic deformation of the hex mesh, but only to plastically deform the material mesh, separately from the elastic deformation.

The hyperelastic computation is currently not fast enough for real-time surgical training scenarios. We therefore do not add and compare plastic rotational deformations for the hyperelastic model. Stretching a bar in interactive simulation allows estimating the loss of realism, if any, that is incurred by using the real-time corotational elastic model in place of the more sophisticated hyperelastic model.

2 Background

Engineers and mathematicians have long debated the relative advantages of tetrahedral vs hexahedral finite elements for modeling elasticity. [8, 9] argue that linear tetrahedral (tet) meshes generate noisy contact pressure and shear stress distributions leading to uneven peak pressures whereas hexahedral meshes exhibit a smooth and more uniform pressure distribution. The authors of [10] state that quadratic tet-elements yield results on par with tri-linear hex-elements (and advocate non-polynomial polyhedral elements in [11]). In practice, linear (total degree) tetrahedral elements and tri-linear elements on hex-partitions are both commonly used for real-time simulation of soft tissue. Tri-linear hex elements perform better over viscous regions, are more flexible, and have higher accuracy than linear tetrahedral elements [12, 13]. SOFA offers

both tet and hex elements for elasticity computations. Partitioning organ models into tetrahedra is well automated (e.g., [14]) whereas quick and reliable coarse hex-meshing remains difficult [15–18]. Moreover, preserving the volume for realistic simulation is more tricky for hex-elements than for linear tet elements: plastically deformed tissue should neither artificially swell nor disappear. The well-known co-rotational FEM [19] models primarily linear elastic stretching in a major direction since it factors out rotational components (the displacement is treated as $\mathbf{R}\hat{\mathbf{x}} - \mathbf{x}$, where $\mathbf{R}$ describes the element rotation, in the notation developed in the next Section). The material point method (MPM, [20–23]) excels at modelling granular plasticity of materials like snow or sand, but not soft tissue, and SPH-type approaches do not take advantage of the available regular quad-offset structure of organs that have a pair of primary directions, e.g., axial and radial for cylinders, forming quadrilateral mesh and whose orthogonal offset naturally yields a regular hexahedral thick shell.

The *linear* elasticity model assumes small strain [24]. To handle large rotations and still use the (low cost) linear model, the *corotational method* [19] factors out large rotations. To extend the model to large non-linear deformations, the *hyperelastic* material [25] bases the stress–strain relationship on one (of many possible) strain energy density functions. This approach requires updating the linear equations solved at each time step and is therefore slower than the linear approaches without global matrix updates.

A plasticity model should include a decomposition rule, a flow rule, yield criteria and a hardening rule [26]. The decomposition rule splits the overall deformation into elastic and plastic components.   The classic approach splits into elastic and plastic deformation using the additive model, $\epsilon = \epsilon^e + \epsilon^p$. While simple, this scheme is accurate only for infinitesimal strains and fails for large deformations. To support compressibility, and for higher numerical stability [27–29] recommend the multiplicative decomposition of the deformation gradient into elastic and plastic factors.   The yield criteria determine the state where the material transits from elastic to the elastoplastic region. In 3D this is a transition surface based on the stress tensor. Commonly-used yield criteria include the Maximum Shear Stress Criterion and the Von Mises yield criterion. The theory of plasticity holds that plastic flow only occurs when the stress stays at the yield surface for some time.   The plastic flow rule describes the plastic strain increment based on plastic flow rate and flow direction. The hardening rule determines how the yield surface changes under plastic deformation. The two common hardening models are the isotropic hardening model that describes the expansion or shrinking of the yield surface, and the kinematic hardening model that preserves the size but moves the center of the yield surface along the strain hardening line.

This paper contributes new aspects to the decomposition rule.

3 Methodology

A material deforms plastically when tensile, bending, compressive or torsion stresses exceed its yield strength. Let $\mathbf{x}$ be the start position, possibly plastically deformed in the previous iterations, and $\hat{\mathbf{x}}$ the deformed position in world space. With $\mathbf{s}$ the reference (domain) coordinates, the gradient $\hat{\mathbf{J}} := [\frac{\partial \hat{\mathbf{x}}_i}{\partial \mathbf{s}_j}]$, characterizes infinitesimal displacement. The deformation gradient

$$\mathbf{F} := \frac{\partial \hat{\mathbf{x}}}{\partial \mathbf{x}} = \frac{\partial \hat{\mathbf{x}}}{\partial \mathbf{s}} \frac{\partial \mathbf{s}}{\partial \mathbf{x}} = \frac{\partial \hat{\mathbf{x}}}{\partial \mathbf{s}} (\frac{\partial \mathbf{x}}{\partial \mathbf{s}})^{-1} = \hat{\mathbf{J}}(\mathbf{J})^{-1} \tag{1}$$

of a deformed hex element with vertices $\mathbf{v}^i$ is denoted $\mathbf{F_o}$ when measured at element center $\mathbf{o} := \sum_i \mathbf{v}^i/2^3$ of the hex, $\mathbf{F}_i$ when measured at vertex i and, for our hyperelastic hexahedral extension, $\mathbf{F}_g$ at each of 8 Gauss points g per hex. Gauss points are optimal sampling points for polynomial quadrature [30]. For plastic deformation, for every hex k and vertex i, we will also compute blended gradients $\overline{\mathbf{F}}_i^k := (\mathbf{F}_i^k + \mathbf{F_o}^k)/2$. This average is inspired by Eq (19) of [6], see the Appendix.
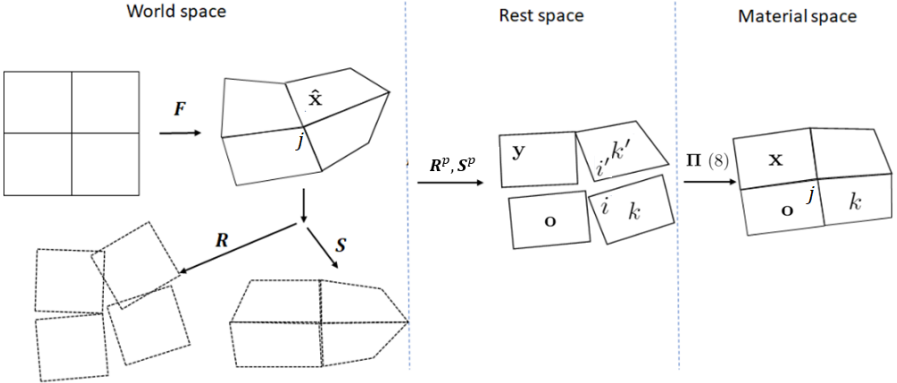

Fig. 4: Quad-mesh analogue to our hex-mesh implementation. (*left*) world space, elastically deformed (where the surgery takes place), (*middle*) rest space (plastically deformed separate elements with local vertices i, i') and (*right*) material space (deformation relaxation to form a consistent mesh).

To support compressibility, for better numerical stability, and since the classic additive (strain) decomposition, $\epsilon = \epsilon^e + \epsilon^p$, holds accurate only for infinitesimal strains and fails for large deformations, [27–29] recommend a multiplicative decomposition of the deformation gradient into elastic and plastic factors.

Plasticity decomposition. The multiplicative decomposition can model incompressibility by enforcing that the determinant of $\mathbf{F}$ does not change. We base our plasticity decomposition on a multiplicative decomposition. We apply

the singular value decomposition $\mathbf{F} = \mathbf{U}\mathbf{D}\mathbf{V}^T$ where $\mathbf{U}, \mathbf{V}$ are orthogonal (rotations or reflections) and $\mathbf{D}$ is a diagonal matrix. Then

$$\mathbf{F} = (\mathbf{U}\mathbf{V}^T)(\mathbf{V}\mathbf{D}\mathbf{V}^T) = \mathbf{R}\mathbf{S}, \tag{2}$$

see Fig. 4, is a factorization of the total deformation $\mathbf{F}$ into a symmetric positive-definite right stretch tensor $\mathbf{S}$, oriented by a polar, orthogonal rotation tensor $\mathbf{R}$. Extracting, in the spirit of [28], the elastic components $\mathbf{R}^e$ of $\mathbf{R}$ and $\mathbf{S}^e$ of $\mathbf{S}$ yields a decomposition into elastic rotation, plastic rotation, elastic stretch and plastic stretch,

$$\mathbf{F} = \mathbf{R}^e\mathbf{R}^p\mathbf{S}^e\mathbf{S}^p. \tag{3}$$

Once the overall deformation is computed, and the elastic component based on either the corotational or a hyperelastic model is removed, the treatment of plasticity is independent of the elastic model. $\mathbf{R}^p$ and $\mathbf{S}^p$ are computed separately, see Fig. 4, middle. This computation of the plastic components also applies to hyperelastic FEM but S^e updates the stiffness matrix at each step.

Plastic stretching. From the blended vertex deformation gradient (for corotational FEM) and the deformation gradient at Gauss points (for hyperelastic FEM), we compute the right Cauchy-Green strain tensor $\mathbf{C} := \mathbf{F}^T\mathbf{F}$, the Green-Lagrangian strain tensor $\mathbf{E} := \frac{1}{2}(\mathbf{C} - \mathbf{I})$ and the *second Piola-Kirchhoff stress tensor* $\boldsymbol{\sigma}$. Akin to [29], the plastic stretch deformation for plastic flow rate ν, plastic yield stress τ, time step Δt with *von Mises stress* $\|\boldsymbol{\sigma}\| := \sqrt{\frac{3}{2}\boldsymbol{\sigma} : \boldsymbol{\sigma}}$ is

$$\mathbf{S}^p := \mathbf{V}(\frac{\mathbf{D}}{(\det \mathbf{D})^{1/3}})^{\gamma}\mathbf{V}^T, \quad \gamma := \min\{\nu\Delta t\frac{\|\boldsymbol{\sigma}\| - \tau}{\|\boldsymbol{\sigma}\|}, 1\}. \tag{4}$$

Plastic rotation for corotational FEM. Splitting $\mathbf{R} = \mathbf{R}^e\mathbf{R}^p$ is nontrivial since the material rotation stems from a combination of shape change such as shear deformation and rigid body rotations [31] making it difficult to uniquely separate out the rigid body rotation. Luckily, in surgical setting, we can neglect inertia-related factors and angular velocity (anatomy does not spin freely), so that plastic rotation can be assumed to solely depend on rotational distortion. We hence measure rotational distortion as the magnitude of the angle based on geodesics on the unit sphere defined as [32]

$$\Phi(\mathbf{R}_1, \mathbf{R}_2) := \|\log(\mathbf{R}_1\mathbf{R}_2^T)\| \in [0, \pi].$$

For the polar decompositions $\mathbf{F}_{\mathbf{o}}^k = \mathbf{R}_{\mathbf{o}}^k\mathbf{U}_{\mathbf{o}}^k$ (at the center $\mathbf{o}$ of hex k) and $\overline{\mathbf{F}}_i^k = \overline{\mathbf{R}}_i^k\overline{\mathbf{U}}_i^k$ (blended at vertex i local to hex k), we compute $\phi_i^k := \Phi(\overline{\mathbf{R}}_i^k, \mathbf{R}_{\mathbf{o}}^k)$.

Omitting the superscript k,

$$\overline{\mathbf{R}}_i^e \, \overline{\mathbf{R}}_i^p = \overline{\mathbf{R}}_i, \quad \overline{\mathbf{R}}_i^e := \overline{\mathbf{R}}_i^{(1-\eta)}, \quad \overline{\mathbf{R}}_i^p := \overline{\mathbf{R}}_i^\eta, \tag{5}$$
$$\eta := \nu^R \Delta t (\phi_i - \tau^R)/(\phi_i + \Phi(\mathbf{I}_3, \mathbf{R_o})),$$

where $\mathbf{I}_3$ is the identity matrix, $\tau^R \in [0, \pi]$ the rotation yield-threshold and $\nu^R \in [0, 1]$ the rotational plastic flow rate.

Computing the plastic rotation per vertex allows for strong distortion. An alternative rigid rotation $\mathbf{R}_\mathbf{o}^p$ at the hex center,

$$\mathbf{R}_\mathbf{o}^e \mathbf{R}_\mathbf{o}^p = \mathbf{R}_\mathbf{o}^{\tilde{\eta}} \mathbf{R}_\mathbf{o}^{1-\tilde{\eta}}, \tag{6}$$
$$\tilde{\eta} := \nu^R \Delta t (\tilde{\phi}^k - \tau^R)/(\tilde{\phi}^k + \Phi(\mathbf{I}_3, \mathbf{R_o})), \quad \tilde{\phi}^k = \max_{i \in \text{hex}^k} \phi_i^k,$$

better preserves element shape, but is less accurate.

Material hardening. We update the plastic yield threshold $\tau \leftarrow \tau + \kappa\gamma\|\boldsymbol{\sigma}\|$ and the rotation yield threshold $\tau^R \leftarrow \tau^R + \kappa\eta\phi_i^k$ to model the isotropic hardening per time step. In the kinematic hardening model the center of the elastic region shifts under deformation. We shift the stress at the center by the stress $\boldsymbol{\sigma}$ at the Gauss node: $\boldsymbol{\alpha} \leftarrow \boldsymbol{\alpha} + \kappa\gamma\frac{\boldsymbol{\sigma}-\boldsymbol{\alpha}}{\|\boldsymbol{\sigma}-\boldsymbol{\alpha}\|}$. The parameter κ controls the amount of work hardening (or softening) per time step.

Plastic update. The rest positions of hex k (see Fig. 4,*middle*) are updated

$$\mathbf{y}_q^k \leftarrow \mathbf{y}_q^k + \mathbf{S}_q^p \mathbf{u}_q \tag{7}$$

where q labels the vertices of the hex in the co-rotational model and the Gauss nodes in the hyperelastic model, $\mathbf{S}_q^p$ is the corresponding plastic stretch and $\mathbf{u}_q := \mathbf{R}_q \hat{\mathbf{x}}_q - \mathbf{x}_q$ is the non-rigid displacement [19].

The rotation map (see Fig. 4) is updated as

$$\text{vertex (Gauss) plastic rotation: } \boldsymbol{\Pi}_q^k \leftarrow \boldsymbol{\Pi}_q^k \, \overline{\mathbf{R}}_q^p, \text{ resp.} \tag{8}$$
$$\text{cell-center plastic rotation: } \boldsymbol{\Pi}^k \leftarrow \boldsymbol{\Pi}^k \, \mathbf{R}_\mathbf{o}^p.$$

Equations (4) and (5) imply that $\det(\mathbf{S}_i^p) = \det(\mathbf{R}_i^p) = 1$. Nevertheless the local element volume can change, because each vertex has a separate plastic offset. Fortunately, the ratio β, of the deformed volume divided by the original volume, can be accurately computed based on the exact volume from the Jacobian $\mathbf{J}$. With short time steps Δt animating the volume restitution, we update

$$\mathbf{y}_i^k \leftarrow \mathbf{y}_i^k + (\mathbf{y}_i^k - \mathbf{o}^k)(1 - \beta)\Delta t. \tag{9}$$

The material space vertex $\mathbf{x}_j$ with global index j surrounded by hexes N_j is updated $\mathbf{x}_j \leftarrow \sum_{k \in N_j} \boldsymbol{\Pi}_q^k \mathbf{y}_q^k / n_j$, where in the corotational model $\mathbf{y}_q^k$ are the n_j vertices corresponding to $\mathbf{x}_j$, and in the hyperelastic model $\mathbf{y}_q^k$ are the n_j

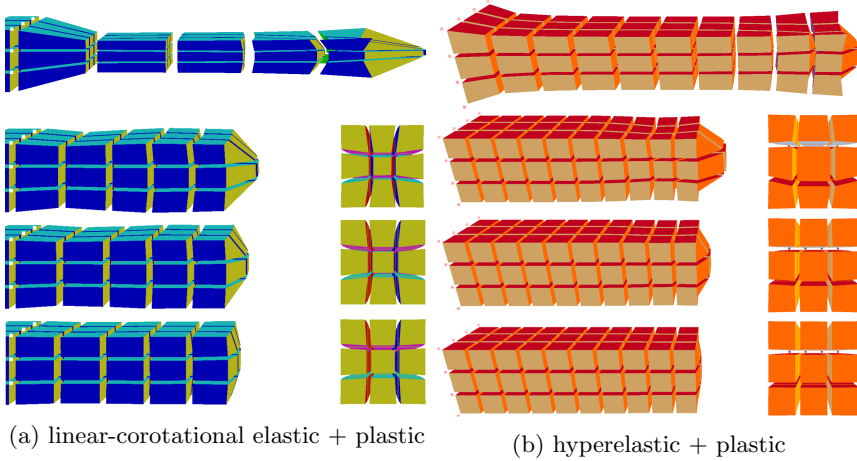(a) linear-corotational elastic + plastic

(b) hyperelastic + plastic

Fig. 5: Stretching test. (*top*) initial stretch. (*bottom* three) deformation for high, medium, low plasticity material. Bars are clamped on the left.

Gauss nodes closest to $\mathbf{x}_j$. see Fig. 4. This fuses the vertices $\mathbf{y}_i^k$ of the elements to form a consistent material.

4 Results and Discussions

Compared to [7], which was based on SOFA 19.12, our new implementation extends SOFA 21.06 and its new Caribou component. In particular, we add hexahedral hyperelastic elements in Caribou. All results are computed on Windows 10 with a i7-9700K CPU and 8G RAM, executing at 80 hex/ms on SOFA v21.06. The time steps immediately after release are the most expensive, adding ca 20% to SOFA's run time for elastic-only co-rotational FEM.

TIPS [5] can now leverage plasticity of anatomical features for laparoscopic surgical procedure training. Tearing of a peritoneal sheet is illustrated in Fig. 3 (a) and plastic free-form deformation in Fig. 3 (b). In (b) a piecewise trilinear function on a coarse hexahedral mesh transforms an embedded much finer mesh.

Fig. 5 compares the stretching of bars consisting of 90-hex elements for two different elastic models and varying parameters τ and ν. The force is applied to the end of the bar at the face center. For co-rotational elasto-plasticity Fig. 5(a) the Young's modulus is 3000, Poisson ratio 0.45 stretching force 350, yield threshold τ (*top* to *bottom*): 1000, 1500, 1500, plastic creep ν: 0.4, 0.2, 0.1. For hyperelastic plasticity Fig. 5(b) the Young's modulus is 3000, Poisson ratio 0.45, (linear) stretching force 1000, yield stress (*top* to *bottom*) 1500, 1800, 2000 and plastic creep: 0.25, 0.2, 0.15. The plastic deformations preserve cross sectional symmetry.

Fig. 6 compares blended vertex plastic rotation and the cell-center plastic rotation by twisting the bar, see (a). In (b) and (c) each row has different
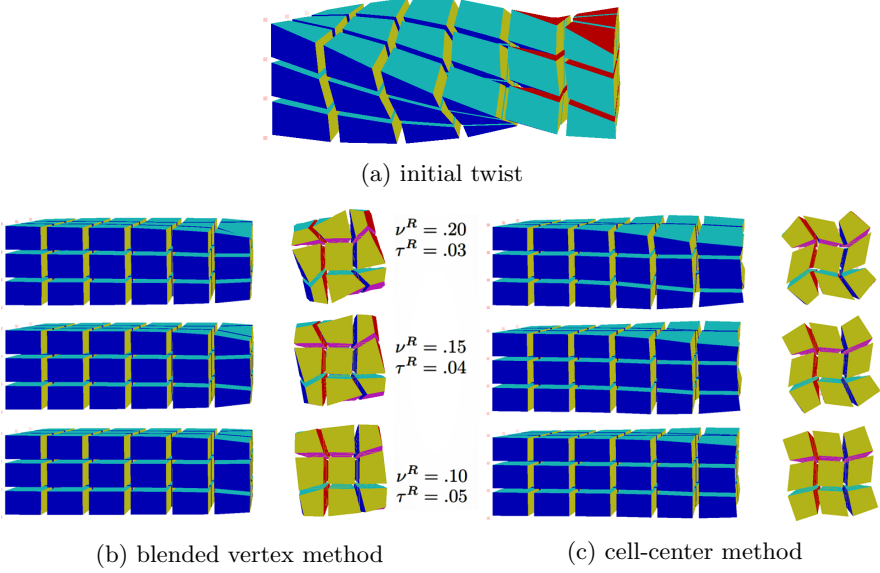
(a) initial twist

$\nu^R = .20$
$\tau^R = .03$

$\nu^R = .15$
$\tau^R = .04$

$\nu^R = .10$
$\tau^R = .05$

(b) blended vertex method   (c) cell-center method

Fig. 6: Twist and plasticity. *top* to *bottom*: high, medium, low rotational plasticity material. (a) initial twist, (b,c) final plastic deformation (side view and cross-section view).

rotational plasticity flow rates ν^R, and rotational plasticity yield thresholds τ^R. The initial twisting force is tangent at all the four edge centers of the bar's end cross-section face. The vertex blending better preserves the cross-sectional shape than the cell-centered approach but distorts each local element more. The cell-centered approach better preserves the local box shape but distorts the cross-sectional view.

For all configurations of Fig. 5 and Fig. 6, the final deformed volume matches with the input volume to less than 1%. The material hardening parameter $\kappa := 0.2$ chosen for all test cases proved effective in preventing ill-shaped material elements during large plastic deformations: the plastic yield threshold is reached and causes fracture before an element becomes too distorted.

Twist torques exerted by lap surgery instrument heads [33] are extremely low. Choosing robustness over exact physics for unrealistic high-torque interactions, our implementation switches off plasticity before an element is inverted. The elastic FEM solver then handles the elements robustly [34].

Fig. 7 compares FEM beam simulations of our method with the Abaqus C3D8R and C3D8 hyperelastic plastic model using Abaqus 8-node hex element with hyperelastic plasticity (Neo-Hookean, C1=833, D1=1E-05) in (a), (c), and our 8-node hex elasto-plasticity (Young'smodulus 5000, Poisson ratio .45) in (b) and (d), and the hyperelastic parameters set to be consistent with linear elasticity for small strain. Fig. 7 shows remarkable agreement on stretch (within 5%) and location of highest deformation during temporal evolution
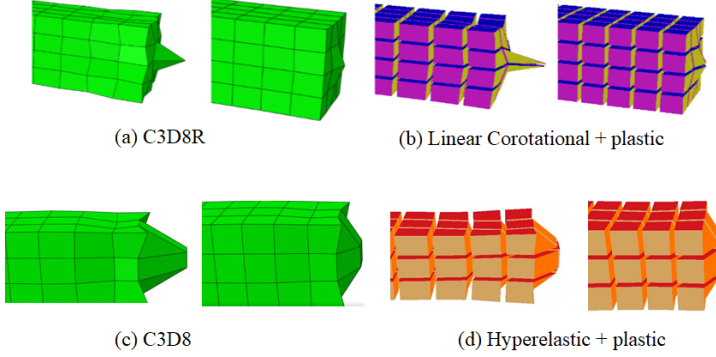
(a) C3D8R

(b) Linear Corotational + plastic

(c) C3D8

(d) Hyperelastic + plastic

Fig. 7: FEM beam simulations: Abaqus (*left*) and our methods (*right*). Final stretch of (a) and (b), respectively (c) and (d) visually agree.

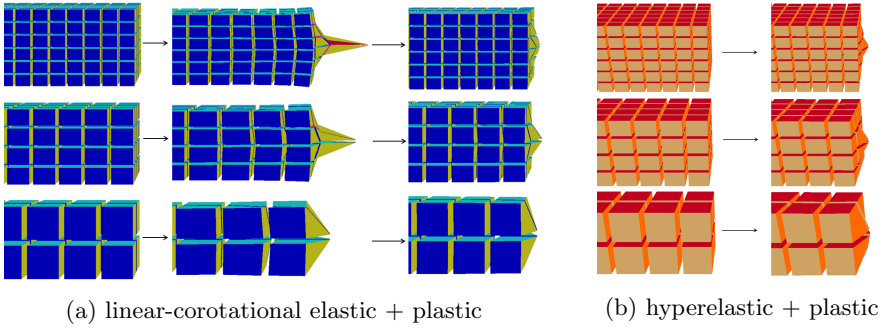(a) linear-corotational elastic + plastic

(b) hyperelastic + plastic

Fig. 8: Stretch refinement tests. (a) Co-rotational elastic (b) Hyperelastic *left*: initial mesh; *right*: final plastic deformation.

between the two models. For one time step of the 90 element bar, the Abaqus model of the beam requires ca. 65 ms (ca. 15 frames per second), our hyperelastic plasticity ca 140 ms (due to updating the stiffness matrix), while our corotational plasticity (no matrix update needed) runs comfortably in real-time at ca. 1 ms per step. Since the hyperelastic model is not currently suitable for real-time surgery simulation, rotational plasticy was not implemented.

Fig. 8 and Fig. 9 analyze behaviour of the models for different levels of granularity. Fig. 8 shows that that applying the same stretch force at the center of the beam cross section results in a visually similar deformation, localized and commensurate with the level of resolution, for co-rotational elastic and hyper-elastic for the regime of forces typical for surgical simulation. Fig. 9 compares outcomes of twisting forces for the blended vertex method and the cell-center method. As in Fig. 6, the trade -off between overall deformation and localized deformation of the hex-elements is apparent. Since all operations are local, e.g. per vertex, and no matrix is assembled to solve, the run time scales linearly with the hexahedra when refining the models.
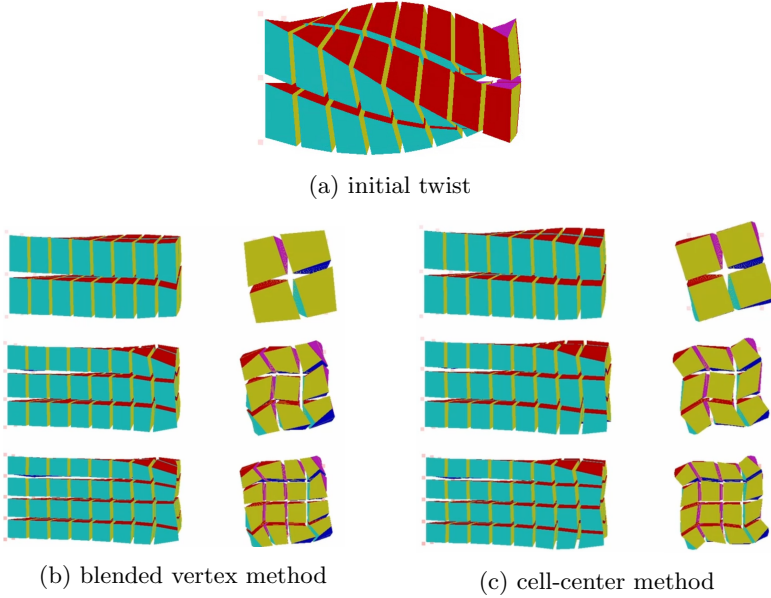
(a) initial twist

(b) blended vertex method

(c) cell-center method

Fig. 9: Twist refinement tests. (a) initial maximal twist (b,c) final plastic deformation (side and cross-section view)

Limitations. To avoid the need for re-meshing our implementation relies on the material hardening to prevent overly distorted elements. Re-meshing is usually also unnecessary because the hex elements are much more flexible than linear tet elements: a coarse hexahedral mesh can handle even the large twist deformation, where as tet elements tend to be much stiffer (see Fig. 10). If the distortion is nevertheless too large, the deformation algorithm switches to purely elastic where elements invert.

To avoid ambiguity on polar rotation, the maximal per-element rotation is capped below π. (The rotational angle of the full object can be much larger, proportional to the number of pieces in the twist axis direction).
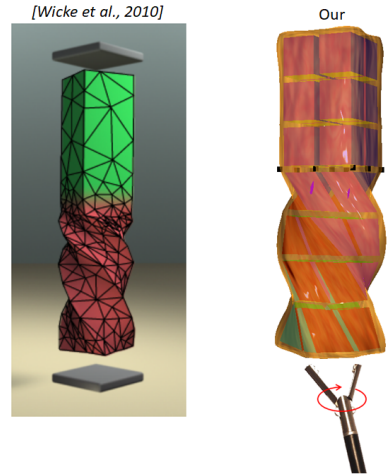

Fig. 10: Twisting comparison *left*: tetrahedral FEM with re-meshing [29] ; *right*: our hexahedral FEM

Code and video availability. The code is to become part of the SOFA distribution. A video demonstration is available at [1].

Declarations

Disclosures and declarations. none. The authors contributed equally.

Competing Interests. none. Neither author has competing interests or funding.

Research involving human participants, their data or biological material. not applicable. The work did not require human or animal studies.

Informed consent. not applicable

Appendix: Blending deformation gradients

Eq (19) of [6] reinterprets, for a tetrahedron with vertices $\mathbf{v}^i$, the third-order accurate 'Phong blending' of the center deformation $\mathbf{F}_o$ and the vertex deformations $\mathbf{F}_i$ as the 'half-gradient' formula: $\sum_i \beta_i\big(\hat{\mathbf{v}}^i + \frac{\mathbf{F}_i}{2}(\mathbf{x} - \mathbf{v}^i)\big)$. Here β_i, short for $\beta_i(\mathbf{x})$, are the barycentric coordinates of $\mathbf{x}$, i.e. $\mathbf{x} = \sum_i \beta_i \mathbf{v}^i$. Then $\sum_i \beta_i(\mathbf{x} - \mathbf{v}^i) = 0$ and, for a constant matrix $\mathbf{F}_o$, $\sum_i \beta_i \mathbf{F}_o(\mathbf{x} - \mathbf{v}^i) = 0$ so that $\sum_i \beta_i\big(\hat{\mathbf{v}}^i + \frac{\mathbf{F}_i + \mathbf{F}_o}{2}(\mathbf{x} - \mathbf{v}^i)\big)$ is an equally valid reformulation of the 'half-gradient' formula. On a hex element with 8 vertices $\mathbf{v}^{ijk}$ and β_q the univariate barycentric coordinates of tri-linear elements $\sum_j \sum_k \sum_l \beta_j \beta_k \beta_l(\mathbf{x} - \mathbf{v}^{ijk}) = 0$ and our tri-hex analogue is $\sum_j \sum_k \sum_l \beta_j \beta_k \beta_l\big(\hat{\mathbf{v}}^i + \frac{\mathbf{F}_i + \mathbf{F}_o}{2}(\mathbf{x} - \mathbf{v}^{ijk})\big)$.

Note that In both the corotational and the hyperelastic approach big rigid body rotations are neutralized prior to averaging $\mathbf{F}_i$ and $\mathbf{F}_0$ so that singularity of $\mathbf{F}_i + \mathbf{F}_o$ due to large rotations is ruled out. In the corotational approach, big rotations are explicitly removed from the deformation gradient. In the hyperelastic approach, the Green strain tensor (E) combines $\mathbf{R}^T \mathbf{R} = \mathbf{I}$, i.e. rotations cancel.

References

[1] Gao, R., Peters, J.: Plastic hexahedral FEM for surgical simulation (video). https://www.youtube.com/watch?v=f0dAL9Bi1VU (2022)

[2] Faure, F., Duriez, C., Delingette, H., Allard, J., Gilles, B., Marchesseau, S., Talbot, H., Courtecuisse, H., Bousquet, G., Peterlik, I., Cotin, S.: SOFA: A Multi-Model Framework for Interactive Physical Simulation. In: Payan, Y. (ed.) Soft Tissue Biomechanical Modeling for Computer Assisted Surgery. Studies in Mechanobiology, Tissue Engineering and Biomaterials, vol. 11, pp. 283–321. Springer, NY (2012). https://doi.org/10.1007/8415_2012_125

[3] Brunet, J.-N.: Exploring new numerical methods for the simulation of soft tissue deformations in surgery assistance. PhD thesis, Université de Strasbourg (2020)

[4] Tarini, M., Hormann, K., Cignoni, P., Montani, C.: Polycube-maps. ACM Trans. Graph. **23**(3), 853–860 (2004)

[5] Sarov, M., Gao, R., Youngquist, J., Sarosi, G., Kurenov, S., Peters, J.: An authoring interface for surgeon-authored VR training. International Journal of Computer Assisted Radiology and Surgery **13**, 1–14273 (2018)

[6] James, D.L.: Phong deformation: a better C^0 interpolant for embedded deformation. ACM Transactions on Graphics (TOG) **39**(4), 56–1 (2020). https://doi.org/10.1145/3386569.3392371

[7] Gao, R., Peters, J.: Improving hexahedral-fem-based plasticity in surgery simulation. In: International Conference on Medical Image Computing and Computer-Assisted Intervention, pp. 571–580 (2021). Springer

[8] Tadepalli, S.C., Erdemir, A., Cavanagh, P.R.: Comparison of hexahedral and tetrahedral elements in finite element analysis of the foot and footwear. Journal of biomechanics **44**(12), 2337–2343 (2011). https://doi.org/10.1016/j.jbiomech.2011.05.006

[9] Benzley, S.E., Perry, E., Merkley, K., Clark, B., Sjaardama, G.: A comparison of all hexagonal and all tetrahedral finite element meshes for elastic and elasto-plastic analysis. In: 4th Itl Meshing Roundtable, vol. 17, pp. 179–191 (1995)

[10] Schneider, T., Hu, Y., Dumas, J., Gao, X., Panozzo, D., Zorin, D.: Decoupling simulation accuracy from mesh quality. ACM ToG **37**(6), 280–128014 (2018)

[11] Schneider, T., Dumas, J., Gao, X., Botsch, M., Panozzo, D., Zorin, D.: Poly-spline finite-element method. ACM ToG **38**(3), 19–11916 (2019)

[12] Shepherd, J.F., Johnson, C.R.: Hexahedral mesh generation constraints. Engineering with Computers **24**(3), 195–213 (2008)

[13] Sarrate Ramos, J., Ruiz-Gironés, E., Roca Navarro, F.J.: Unstructured and semi-structured hexahedral mesh generation methods. Computational Technology Reviews **10**, 35–64 (2014)

[14] Hu, Y., Schneider, T., Wang, B., Zorin, D., Panozzo, D.: Fast tetrahedral meshing in the wild. ACM Trans. Graph **39**(4), 117 (2020)

[15] Blacker, T.D.: Automated conformal hexahedral meshing constraints,

challenges and opportunities. Eng. Comput **17**(3), 201–210 (2001)

[16] Liu, H., Zhang, P., Chien, E., Solomon, J., Bommes, D.: Singularity-constrained octahedral fields for hexahedral meshing. ACM Trans. Graph **37**(4), 93–19317 (2018)

[17] Cherchi, G., Alliez, P., Scateni, R., Lyon, M., Bommes, D.: Selective padding for polycube-based hexahedral meshing. Comput. Graph. Forum **38**(1), 580–591 (2019)

[18] Gao, X., Shen, H., Panozzo, D.: Feature preserving octree-based hexahedral meshing. Comput. Graph. Forum **38**(5), 135–149 (2019)

[19] Hauth, M., Strasser, W.: Corotational simulation of deformable solids (2004)

[20] Schreck, C., Wojtan, C.: A practical method for animating anisotropic elastoplastic materials. In: Comp Gr Forum, vol. 39, pp. 89–99 (2020)

[21] Wolper, J., Fang, Y., Li, M., Lu, J., Gao, M., Jiang, C.: Cd-mpm: continuum damage material point methods for dynamic fracture animation. ACM Transactions on Graphics (TOG) **38**(4), 1–15 (2019)

[22] Stomakhin, A., Schroeder, C., Chai, L., Teran, J., Selle, A.: A material point method for snow simulation. ACM TOG **32**(4), 1–10 (2013)

[23] Wang, S., Ding, M., Gast, T.F., Zhu, L., Gagniere, S., Jiang, C., Teran, J.M.: Simulation and visualization of ductile fracture with the material point method. Proc ACM Comp Gr & Interactive Tech **2**(2), 1–20 (2019)

[24] Wikipedia contributors: Elasticity (physics) — Wikipedia, The Free Encyclopedia. [Online; accessed 30-April-2022] (2022). https://en.wikipedia.org/w/index.php?title=Elasticity_(physics)&oldid=1083886093

[25] Wikipedia contributors: Hyperelastic material — Wikipedia, The Free Encyclopedia. [Online; accessed 30-April-2022] (2022). https://en.wikipedia.org/w/index.php?title=Hyperelastic_material&oldid=1074750583

[26] Wikipedia contributors: Plasticity (physics) — Wikipedia, The Free Encyclopedia. [Online; accessed 30-April-2022] (2022). https://en.wikipedia.org/w/index.php?title=Plasticity_(physics)&oldid=1068367824

[27] Irving, G., Teran, J., Fedkiw, R.: Invertible finite elements for robust simulation of large deformation. In: Proceedings of the 2004 ACM SIGGRAPH/Eurographics Symp. Comp. Animation, pp. 131–140 (2004)

[28] Bargteil, A.W., Wojtan, C., Hodgins, J.K., Turk, G.: A finite element

method for animating large viscoplastic flow. ACM ToG **26**(3), 16 (2007)

[29] Wicke, M., Ritchie, D., Klingner, B.M., Burke, S., Shewchuk, J.R., O'Brien, J.F.: Dynamic local remeshing for elastoplastic simulation. ACM Transactions on graphics (TOG) **29**(4), 1–11 (2010)

[30] Wikipedia contributors: Gaussian quadrature — Wikipedia, The Free Encyclopedia. [Online; accessed 30-April-2022] (2022). https://en.wikipedia.org/w/index.php?title=Gaussian_quadrature& oldid=1083985268

[31] Holmedal, B.: Spin and vorticity with vanishing rigid-body rotation during shear in continuum mechanics. J Mech & and Phys of Solids **137**, 103835 (2020)

[32] Huynh, D.Q.: Metrics for 3d rotations: Comparison and analysis. Journal of Mathematical Imaging and Vision **35**(2), 155–164 (2009)

[33] Richards, C., Rosen, J., Hannaford, B., Pellegrini, C.A., Sinanan, M.N.: Skills evaluation in minimally invasive surgery using force/torque signatures. Surgical endoscopy **14**(9), 791–798 (2000). https://doi.org/10. 1007/s004640000230

[34] Irving, G., Teran, J., Fedkiw, R.: Tetrahedral and hexahedral invertible finite elements. Graphical Models **68**(2), 66–89 (2006)